Few-mode fiber, splice and SDM component characterization by spatially-diverse optical vector network analysis

Research Article | Vol. 25, No. 19 | 18 Sep 2017 | OPTICS EXPRESS 22347
Optics EXPRESS

Few-mode fiber, splice and SDM component characterization by spatially-diverse optical vector network analysis

SIMON ROMMEL,[1,2,*] JOSÉ MANUEL DELGADO MENDINUETA,[1] WERNER KLAUS,[1] JUN SAKAGUCHI,[1] JUAN JOSÉ VEGAS OLMOS,[3] YOSHINARI AWAJI,[1] IDELFONSO TAFUR MONROY,[2] AND NAOYA WADA[1]

[1]*Photonic Network System Laboratory, National Institute of Information and Communications Technology (NICT), 4-2-1 Nukui-Kitamachi, Koganei, Tokyo 184-8795, Japan*
[2]*Department of Photonics Engineering, Technical University of Denmark, 2800 Kgs. Lyngby, Denmark*
[3]*Mellanox Technologies, Ledreborg Allé 130B, 4000 Roskilde, Denmark*
[*]*sirem@fotonik.dtu.dk*

Abstract: This paper discusses spatially diverse optical vector network analysis for space division multiplexing (SDM) component and system characterization, which is becoming essential as SDM is widely considered to increase the capacity of optical communication systems. Characterization of a 108-channel photonic lantern spatial multiplexer, coupled to a 36-core 3-mode fiber, is experimentally demonstrated, extracting the full impulse response and complex transfer function matrices as well as insertion loss (IL) and mode-dependent loss (MDL) data. Moreover, the mode-mixing behavior of fiber splices in the few-mode multi-core fiber and their impact on system IL and MDL are analyzed, finding splices to cause significant mode-mixing and to be non-negligible in system capacity analysis.

OCIS codes: (120.3180) Interferometry; (060.4230) Multiplexing; (060.4510) Optical communications.

References and links

1. D. J. Richardson, J. M. Fini, and L. E. Nelson, "Space-division multiplexing in optical fibres," Nat. Photonics **7**, 354–362 (2013).
2. X. Liu, S. Chandrasekhar, X. Chen, P. Winzer, Y. Pan, B. Zhu, T. Taunay, M. Fishteyn, M. Yan, J. M. Fini, E. Monberg, and F. Dimarcello, "1.12-Tb/s 32-QAM-OFDM superchannel with 8.6-b/s/Hz intrachannel spectral efficiency and space-division multiplexing with 60-b/s/Hz aggregate spectral efficiency," in *Proceedings of the European Conference on Optical Communications* (OSA, 2011), Th.13.B.1.
3. S. Randel, R. Ryf, A. Gnauck, M. A. Mestre, C. Schmidt, R. Essiambre, P. Winzer, R. Delbue, P. Pupalaikis, A. Sureka, Y. Sun, X. Jiang, and R. Lingle, "Mode-multiplexed 620-GBd QPSK transmission over 1200-km DGD-compensated few-mode fiber," in *Proceedings of the Optical Fiber Communication Conference* (OSA, 2012), PDP5C.5.
4. T. Mizuno, H. Takara, K. Shibahara, A. Sano, and Y. Miyamoto, "Dense space division multiplexed transmission over multicore and multimode fiber for long-haul transport systems," J. Lightw. Technol. **34**, 1484–1493 (2016).
5. W. Klaus, B. J. Puttnam, R. S. Luís, J. Sakaguchi, J.-M. D. Mendinueta, Y. Awaji, and N. Wada, "Advanced space division multiplexing technologies for optical networks," J. Opt. Commun. Netw. **9**, C1–C11 (2017).
6. J. Sakaguchi, W. Klaus, J. M. Delgado Mendinueta, B. J. Puttnam, R. S. Luis, Y. Awaji, N. Wada, T. Hayashi, T. Nakanishi, T. Watanabe, Y. Kokubun, T. Takahata, and T. Kobayashi, "Large spatial channel (36-core 3 mode) heterogeneous few-mode multicore fiber," J. Lightw. Technol. **34**, 93–103 (2016).
7. P. J. Winzer and G. J. Foschini, "MIMO capacities and outage probabilities in spatially multiplexed optical transport systems," Opt. Express **19**, 16680–16696 (2011).
8. K.-P. Ho and J. M. Kahn, "Linear propagation effects in mode-division multiplexing systems," J. Lightw. Technol. **32**, 614–628 (2014).
9. T. Sakamoto, T. Matsui, K. Saitoh, S. Saitoh, K. Takenaga, T. Mizuno, Y. Abe, K. Shibahara, Y. Tobita, S. Matsuo, K. Aikawa, S. Aozasa, K. Nakajima, and Y. Miyamoto, "Low-loss and Low-DMD 6-mode 19-core fiber with cladding diameter of less than 250 μm," J. Lightw. Technol. **35**, 443–449 (2017).
10. T. Hayashi, T. Nagashima, K. Yonezawa, Y. Wakayama, D. Soma, K. Igarashi, T. Tsuritani, T. Taru, and T. Sasaki, "Six-mode 19-core fiber with 114 spatial modes for weakly-coupled mode-division-multiplexed transmission," J. Lightw. Technol. **35**, 748–754 (2017).

#297941 https://doi.org/10.1364/OE.25.022347
Journal © 2017 Received 15 Jun 2017; revised 28 Aug 2017; accepted 31 Aug 2017; published 6 Sep 2017

11. N. K. Fontaine, "Characterization of space-division multiplexing fibers using swept-wavelength interferometry," in *Proceedings of the Optical Fiber Communication Conference* (OSA, 2015), W4I.7.
12. E. Awwad, G. R.-B. Othman, and Y. Jaouën, "Space-time coding schemes for MDL-impaired mode-multiplexed fiber transmission systems," J. Lightw. Technol. **33**, 5084–5094 (2015).
13. C. Okonkwo, R. van Uden, H. Chen, H. de Waardt, and T. Koonen, "Advanced coding techniques for few mode transmission systems," Opt. Express **23**, 1411–1420 (2015).
14. N. K. Fontaine and R. Ryf, "Characterization of mode-dependent loss of laser inscribed photonic lanterns for space division multiplexing systems," in *Proceedings of the OptoElectronics and Communications Conference and Photonics in Switching* (IEICE, 2013), MR2–2.
15. J. M. Delgado Mendinueta, W. Klaus, J. Sakaguchi, Y. Awaji, and N. Wada, "Numerical investigation of equalization enhanced phase noise penalties for MQAM modulations in few-mode fiber transmission with time domain equalization," in *Proceedings of Photonic Networks and Devices* (OSA, 2017), NeTu2B.1.
16. S. Warm and K. Petermann, "Splice loss requirements in multi-mode fiber mode-division-multiplex transmission links," Opt. Express **21**, 519–532 (2013).
17. S. Rommel, J. M. Delgado Mendinueta, W. Klaus, J. Sakaguchi, J. J. Vegas Olmos, Y. Awaji, I. Tafur Monroy, and N. Wada, "Analysis of few-mode multi-core fiber splice behavior using an optical vector network analyzer," in *Proceedings of the European Conference on Optical Communications* (IEEE, 2017), W.3.B.5.
18. W. Klaus, S. Rommel, J. M. Delgado Mendinueta, J. Sakaguchi, P. Mitchell, N. Psaila, J. J. Vegas Olmos, I. Tafur Monroy, Y. Awaji, and N. Wada, "Numerical analysis of misalignment effects in few-mode multi-core fiber systems," in *Proceedings of the IEEE Photonics Conference* (IEEE, 2017), TuD2.3.
19. F. Ferreira, D. Fonseca, A. Lobato, B. Inan, and H. Silva, "Reach improvement of mode division multiplexed systems using fiber splices," IEEE Photonics Technol. Lett. **25**, 1091–1094 (2013).
20. G. VanWiggeren, A. Motamedi, and D. Baney, "Single-scan interferometric component analyzer," IEEE Photonics Technol. Lett. **15**, 263–265 (2003).
21. D. K. Gifford, B. J. Soller, M. S. Wolfe, and M. E. Froggatt, "Optical vector network analyzer for single-scan measurements of loss, group delay, and polarization mode dispersion," Appl. Opt. **44**, 7282–7286 (2005).
22. N. K. Fontaine, R. Ryf, M. A. Mestre, B. Guan, X. Palou, S. Randel, Y. Sun, L. Gruner-Nielsen, R. V. Jensen, and R. Lingle, "Characterization of space-division multiplexing systems using a swept-wavelength interferometer," in *Proceedings of the Optical Fiber Communication Conference* (OSA, 2013), OW1K.2.
23. J. Bohn, J. Carpenter, S. Gross, M. J. Withford, and J. Schröder, "Characterization of laser inscribed on-chip photonic lanterns with different core distances," in *Proceedings of the European Conference on Optical Communications* (IEEE, 2015).
24. S. Rommel, J. M. Delgado Mendinueta, W. Klaus, J. Sakaguchi, J. J. Vegas Olmos, Y. Awaji, I. Tafur Monroy, and N. Wada, "Impulse response of a 36-core few-mode photonic lantern hybrid spatial-multiplexer," in *Proceedings of Extremely Advanced Transmission Technologies* (IEICE, 2017), P–4.
25. S. Rommel, J. M. Delgado Mendinueta, W. Klaus, J. Sakaguchi, J. J. Vegas Olmos, Y. Awaji, I. Tafur Monroy, and N. Wada, "Characterization of a fiber-coupled 36-core 3-mode photonic lantern spatial multiplexer," in *Proceedings of Photonic Networks and Devices* (OSA, 2017), NeW3B.2.
26. B. J. Soller, D. K. Gifford, M. S. Wolfe, and M. E. Froggatt, "High resolution optical frequency domain reflectometry for characterization of components and assemblies," Opt. Express **13**, 666–674 (2005).
27. G. VanWiggeren and D. Baney, "Swept-wavelength interferometric analysis of multiport components," IEEE Photonics Technol. Lett. **15**, 1267–1269 (2003).
28. G. H. Golub and C. Reinsch, "Singular value decomposition and least squares solutions," Numer. Math. **14**, 403–420 (1970).
29. B. L. Heffner, "Accurate, automated measurement of differential group delay dispersion and principal state variation using Jones matrix eigenanalysis," IEEE Photonics Technol. Lett. **5**, 814–817 (1993).
30. R. Maruyama, N. Kuwaki, S. Matsuo, and M. Ohashi, "Relationship between mode coupling and fiber characteristics in few-mode fibers analyzed using impulse response measurements technique," J. Lightw. Technol. **35**, 650–657 (2017).
31. P. Mitchell, G. Brown, R. R. Thomson, N. Psaila, and A. Kar, "57 channel (19x3) spatial multiplexer fabricated using direct laser inscription," in *Proceedings of the Optical Fiber Communication Conference* (OSA, 2014), M3K.5.

1. Introduction

As fiber optic communication links rapidly approach the limit of conventional single mode fibers (SMF) of around 100 Tbit/s, space division multiplexing (SDM) has recently been introduced to increase the available transmission capacity [1–6]. Few-mode fibers (FMFS) supporting multiple spatial modes allow transmission of a number of channels on an orthogonal set of modes of the FMF, at the cost of requiring multiple-input multiple-output (MIMO) equalization to invert the mode-mixing that takes place at (de-)multiplexers, at fiber splice points and during propagation through the fiber [6–8]. Multi-core fibers (MCFS) reduce the footprint and increase capacity at the

Optics EXPRESS

cost of introducing inter-core crosstalk [5] and combined with mode-multiplexing form few-mode multi-core fibers (FM-MCF) which make spatial channel counts above 100 feasible [6, 9, 10].

An SDM system using single- or multi-core FMFs consists of a bank of transmitters, connected to a spatial multiplexer (SMUX), followed by an SDM fiber transmission span, a de-multiplexer and finally a bank of coherent receivers. The transmission span may be a simple fiber link, but may also include more complex subsystems such as switches, and amplifiers [11]. Additionally, a fusion splice every few km will be unavoidable in practical SDM systems. To model such systems and estimate their performance in terms of capacity, MIMO complexity and energy consumption, accurate knowledge of the characteristics such as insertion loss (IL), mode-dependent loss (MDL) and differential modal group delay (DMD), of the involved components is essential [7, 8].

For the MIMO equalizer to recover the original signals despite significant mode-mixing in FM-MCFS, mode-dependent loss (MDL) must be small, while mode scrambling at the transmitter improves tolerance to system MDL [7] without requiring additional coding which may also improve tolerance to MDL [12, 13]. System capacity is maximized if all modes supported by the fiber are used to transmit information [7, 14]. Thus, an SMUX should excite all the available orthogonal modes and should have low insertion loss (IL) to preserve optical power and low MDL to maintain MIMO processing performance by avoiding eigenmode signal-to-noise ratio (SNR) degradation. The fiber DMD determines the spread between signal components and thus sets a lower limit to MIMO equalizer complexity. It may further degrade system performance due to equalization enhanced phase noise [15]. Fusion splices within FMFS—and in particular FM-MCFS—not only introduce IL, but may also introduce significant amounts of mode-mixing and MDL [16–18]. While splices may severely degrade system performance due to their IL and additional MDL, their mode mixing behavior may potentially reduce overall system MDL, to the point where artificial introduction of splices has been considered for reach increase in FMF transmission systems [16, 19].

Optical vector network analysis, based on swept wavelength interferometry—where light from a wavelength swept source is sent through an interferometric structure containing the device under test (DUT) and as a result at the receiver creates interference fringes according to the device response—allows direct measurement of the impulse response and the complex transfer function of an optical device or system [20, 21]. More recently, spatially diverse optical vector network analyzer (SDM-OVNA) setups have been introduced, allowing measurement of the temporal and spectral response of FMFS [11, 22], as well as characterization of SDM system components [14, 23, 24]. The mode-mixing at fiber splices and their impact on system IL and MDL was investigated by the authors in [17, 25], based on analysis of the impulse response and comparison of measurements with different splices. A complete description of the SDM-OVNA setup and especially the required digital signal processing (DSP) is however not found in the literature.

In this article, the authors provide a comprehensive discussion of the operating principle of spatially diverse optical vector network analysis and the DSP required to extract the impulse response and complex transfer function matrices as well as the linear parameters (such as IL, MDL and DMD) of the device or system under test. The authors present extended characterization results for the characterization of a 3D waveguide photonic lantern SMUX for a 36-core 3-mode fiber, as well as for the behavior of fusion splices in FM-MCFS [17, 24, 25]. Full characterization of the photonic lantern SMUX is performed using a reflective SDM-OVNA setup, measuring its impulse response and complex transfer function matrices as well as IL and MDL for all cores. Using the SMUX as a basis, the mode-mixing behavior and impact on system IL and MDL is analyzed for different fusion splices and cleaves. Through the extended analysis, separating the impact of fiber splice and cleave, the accuracy of characterization is significantly improved and both are found to have significant impact on IL and MDL. These results confirm spatially diverse optical vector network analysis to be a potent tool for accurate characterization of SDM systems and

Optics EXPRESS

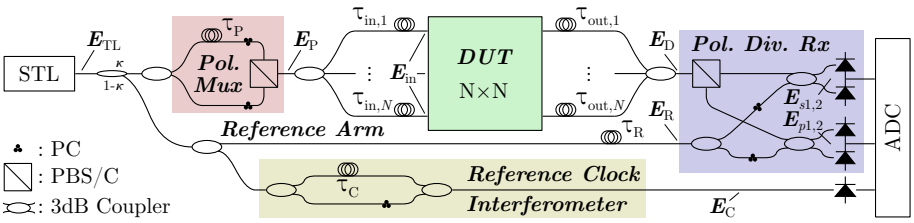

Fig. 1. General SDM-OVNA setup, including reference clock interferometer. STL: wavelength swept tunable laser, PC: polarization controller, PBS/C: polarization beam splitter/combiner, DUT: device under test, ADC: analog to digital converter.

components and by characterizing the impact of splices in FM-MCF allow improved modeling and capacity estimation of SDM systems with a large channel count.

The remainder of this article is organized as follows: section 2 discusses spatially diverse optical vector network analysis, providing a comprehensive discussion of the SDM-OVNA setup, the principle of operation and the required DSP for complete characterization of the device under test. Section 3 discusses the measurements performed and the results obtained, first characterizing the photonic lantern SMUX, then showing how fiber DMD and mode-mixing behavior at discrete mode-mixing points in the fiber can be derived from the measured impulse response and finally analyzing the impact of fiber splices and the cleaved fiber facet used in reflective OVNA measurements on system IL and MDL. Section 4 summarizes and concludes the article.

2. Spatially-diverse optical vector network analysis – principle of operation and digital signal processing

Swept wavelength interferometry allows measurement of the polarization resolved complex transfer function $\boldsymbol{H}(\omega)$ and impulse response $\boldsymbol{h}(t)$ of an optical device under test [20, 26]. To measure the full transfer function matrix of a multiport, space division multiplexing (SDM) system or component, the scheme may be extended to form a spatially diverse optical vector network analyzer (SDM-OVNA) [22, 25, 27]. This section presents the setup and principle of operation of an SDM-OVNA for the analysis of an SDM system or component with $N \times N$ ports in section 2.1 and discusses the digital signal processing (DSP) for measurement of the impulse response, complex transfer function and linear parameters (such as insertion loss (IL), mode-dependent loss (MDL), differential modal group delay (DMD) and mode coupling) of the system or component in section 2.2. Finally, section 2.3 presents a reflective SDM-OVNA setup allowing isolated characterization of single SDM devices or components.

2.1. Spatially-diverse optical vector network analysis setup

The basic setup for a spatially diverse OVNA for transmissive characterization of a device with $N \times N$ ports is shown in Fig. 1. It consists of a wavelength swept tunable laser (STL), followed by an interferometric structure with one arm containing the device under test (DUT) and the other arm serving as reference. While the setup in Fig. 1 is designed to measure the transmission characteristics of the DUT, the use of circulators at the input to the DUT allows measuring its reflective characteristics or, using the reflection from a cleaved fiber facet, to measure transmission characteristics in a reflective manner as discussed in section 2.3.

For polarization resolved measurement, a polarization multiplexing unit generates a signal of two orthogonal polarizations with a relative delay τ_p. The signal is split into N copies, to which differential delays $\tau_{in,1}$ to $\tau_{in,N}$ are applied before input to the DUT. Another set of differential delays $\tau_{out,1}$ to $\tau_{out,N}$ are applied to the output of the DUT before combining the N outputs, beating them with the signal from the reference arm on a polarization diverse receiver and

recording the resulting interference signals. An additional interferometer with delay τ_C generates a reference signal used to correct for deviations in sweep speed and convert the linear sweep in wavelength performed by the STL into a linear sweep in frequency as required for extraction of the DUT response.

Assuming the optical field $\boldsymbol{E}_{\text{STL}}$ generated by the STL is

$$\boldsymbol{E}_{\text{STL}} = A\,\mathrm{e}^{-j\omega(t)t}\,\boldsymbol{p}_{\text{STL}}, \tag{1}$$

where $\boldsymbol{p}_{\text{STL}}$ is a unit vector representing input polarization orientation, A is the complex field amplitude and $\omega(t) = 2\pi c/\left(\lambda_0 + v_{\text{sweep}}t\right)$ is the angular optical frequency resulting from a linear sweep of laser wavelength, starting at λ_0 and with speed v_{sweep}; c being the speed of light in vacuum. The signal after the polarization multiplexer may then be expressed as

$$\boldsymbol{E}_{\text{P}} = \sqrt{\frac{\kappa}{2}}A\,\mathrm{e}^{-j\omega(t)t}\left[\boldsymbol{R}_{\text{P},s}\boldsymbol{p}_{\text{STL}} + \mathrm{e}^{j\omega(t)\tau_{\text{P}}}\,\boldsymbol{R}_{\text{P},p}\boldsymbol{p}_{\text{STL}}\right], \tag{2}$$

where $\boldsymbol{R}_{\text{P},s}$ and $\boldsymbol{R}_{\text{P},p}$ are 2×2 polarization rotation matrices, that align $\boldsymbol{E}_{\text{STL}}$ to the polarization axes of the polarization beam combiner (PBC) and the factor $\sqrt{\kappa/2}$ results from the two splitters. Without loss of generality and to simplify notation in the following, we assume the polarization axes of the PBC to be the standard basis, simplifying Eq. (2) to

$$\boldsymbol{E}_{\text{P}} = \sqrt{\frac{\kappa}{2}}A\,\mathrm{e}^{-j\omega(t)t}\left[\begin{pmatrix}1\\0\end{pmatrix} + \mathrm{e}^{j\omega(t)\tau_{\text{P}}}\begin{pmatrix}0\\1\end{pmatrix}\right] = \sqrt{\frac{\kappa}{2}}A\begin{pmatrix}\mathrm{e}^{-j\omega(t)t}\\ \mathrm{e}^{-j\omega(t)(t-\tau_{\text{P}})}\end{pmatrix} = \sqrt{\frac{\kappa}{2}}A\boldsymbol{E}_{2\text{P}}. \tag{3}$$

The N copies of the polarization multiplexed signal at the input to the DUT may then be expressed in a combined notation as the product of a $2N\times 1$ vector $\boldsymbol{E}_{2\text{NP}}$ with elements $(\boldsymbol{E}_{2\text{P}}^T,\ldots,\boldsymbol{E}_{2\text{P}}^T)^T$, a $2N\times 2N$ block diagonal matrix $\boldsymbol{R}_{\text{in}}$ consisting of a set of complex, unitary, independent 2×2 polarization rotation matrices $\boldsymbol{R}_{\text{in},1}$ to $\boldsymbol{R}_{\text{in},N}$ (as highlighted in Eq. (4)) and a $2N\times 2N$ diagonal matrix $\boldsymbol{D}_{\text{in}}$ with the delays $d_{\text{in},i} = \mathrm{e}^{j\omega(t)\tau_{\text{in},i}}$:

$$\begin{aligned}\boldsymbol{E}_{\text{in}} &= \sqrt{\frac{\kappa}{2N}}A\begin{bmatrix}\boldsymbol{R}_{\text{in},1} & & 0\\ & \ddots & \\ 0 & & \boldsymbol{R}_{\text{in},N}\end{bmatrix}\begin{bmatrix}d_{\text{in},1} & 0 & & & 0\\ 0 & d_{\text{in},1} & & & \\ & & \ddots & & \\ & & & d_{\text{in},N} & 0\\ 0 & & & 0 & d_{\text{in},N}\end{bmatrix}\begin{pmatrix}\mathrm{e}^{-j\omega(t)t}\\ \mathrm{e}^{-j\omega(t)(t-\tau_{\text{P}})}\\ \vdots\\ \mathrm{e}^{-j\omega(t)t}\\ \mathrm{e}^{-j\omega(t)(t-\tau_{\text{P}})}\end{pmatrix}\\ &= \sqrt{\frac{\kappa}{2N}}A\boldsymbol{R}_{\text{in}}\boldsymbol{D}_{\text{in}}\boldsymbol{E}_{2\text{NP}}.\end{aligned} \tag{4}$$

E_{in} thus effectively contains $2N$ scaled and shifted copies of the original swept optical signal and the N pairs with differential delay τ_{P} are applied to the N inputs of the DUT. Expressing the $(2N)^2$ complex transfer functions $H_{k,l}(\omega)$ (with $k,l\in[1,2N]$) relating the polarizations of each of the N input ports to the polarizations of each of the N output ports of the DUT in a $2N\times 2N$ matrix $\boldsymbol{H}(\omega)$, allows writing the output signal of the upper arm of the main interferometer as

$$\boldsymbol{E}_{\text{D}} = \frac{\sqrt{\kappa}}{\sqrt{2}N}A\sum_{2\times 1}\boldsymbol{D}_{\text{out}}\boldsymbol{R}_{\text{out}}\boldsymbol{H}(\omega)\boldsymbol{R}_{\text{in}}\boldsymbol{D}_{\text{in}}\boldsymbol{E}_{2\text{NP}}, \tag{5}$$

where $\boldsymbol{D}_{\text{out}}$ and $\boldsymbol{R}_{\text{out}}$ are the delays and polarization rotations after the different outputs of the DUT, defined in the same way as $\boldsymbol{D}_{\text{in}}$ and $\boldsymbol{R}_{\text{in}}$ in Eq. (4). Further, $\sum_{2\times 1}$ is a summation over pairs of rows of the $2N\times 1$ vector resulting from the matrix multiplication in Eq. (5), such that

$$\boldsymbol{E}_{\text{D}} = \frac{\sqrt{\kappa}}{\sqrt{2}N}A\begin{pmatrix}\sum_{k,l=1}^{N}\left[\hat{H}_{2k-1,2l-1}\,\mathrm{e}^{-j\omega(t)(t-\tau_{\text{out},k}-\tau_{\text{in},l})} + \hat{H}_{2k-1,2l}\,\mathrm{e}^{-j\omega(t)(t-\tau_{\text{out},k}-\tau_{\text{in},l}-\tau_{\text{P}})}\right]\\ \sum_{k,l=1}^{N}\left[\hat{H}_{2k,2l-1}\,\mathrm{e}^{-j\omega(t)(t-\tau_{\text{out},k}-\tau_{\text{in},l})} + \hat{H}_{2k,2l}\,\mathrm{e}^{-j\omega(t)(t-\tau_{\text{out},k}-\tau_{\text{in},l}-\tau_{\text{P}})}\right]\end{pmatrix}, \tag{6}$$

where the unitary polarization rotations $\boldsymbol{R}_{\text{in}}$ and $\boldsymbol{R}_{\text{out}}$ have been combined with $\boldsymbol{H}(\omega)$ into $\hat{\boldsymbol{H}}(\omega) = \boldsymbol{R}_{\text{out}}\boldsymbol{H}(\omega)\boldsymbol{R}_{\text{in}}$ with the $(2N)^2$ complex elements $\hat{H}_{k,l}(\omega)$, where $k, l \in [1, 2N]$.

The signal in the reference arm undergoes delay τ_{R} and at the input of the polarization diverse receiver is

$$\boldsymbol{E}_{\text{R}} = \sqrt{\frac{1-\kappa}{2}} A\, \mathrm{e}^{-j\omega(t)(t-\tau_{\text{R}})}\, \boldsymbol{R}_{\text{R}}\boldsymbol{p}_{\text{STL}}, \tag{7}$$

where $\boldsymbol{R}_{\text{R}}$ represents a random polarization rotation along the fiber.

Splitting $\boldsymbol{E}_{\text{D}}$ from Eq. (6) into orthogonal polarizations represented by unit vectors $\boldsymbol{s}$ and $\boldsymbol{p}$ using a polarization beam splitter (PBS) as

$$\boldsymbol{E}_{\text{D},s} = (\boldsymbol{E}_{\text{D}} \cdot \boldsymbol{s})\, \boldsymbol{s} \qquad \text{and} \qquad \boldsymbol{E}_{\text{D},p} = (\boldsymbol{E}_{\text{D}} \cdot \boldsymbol{p})\, \boldsymbol{p} \tag{8}$$

and combining each with a polarization-aligned half of the reference signal $\boldsymbol{E}_{\text{R}}$ gives the incident fields on the two balanced photodetectors:

$$\boldsymbol{E}_{s1,2} = \frac{1}{\sqrt{2}}\boldsymbol{E}_{\text{D},s} + \frac{1}{2}\boldsymbol{E}_{\text{R}}\boldsymbol{R}_{\text{R},s} = \frac{1}{2}\left[\sqrt{2}\boldsymbol{E}_{\text{D}} \cdot \boldsymbol{s} + \sqrt{\frac{1-\kappa}{2}} A\, \mathrm{e}^{-j\omega(t)(t-\tau_{\text{R}})}\right]\boldsymbol{s} \tag{9}$$

$$\boldsymbol{E}_{p1,2} = \frac{1}{\sqrt{2}}\boldsymbol{E}_{\text{D},p} + \frac{1}{2}\boldsymbol{E}_{\text{R}}\boldsymbol{R}_{\text{R},p} = \frac{1}{2}\left[\sqrt{2}\boldsymbol{E}_{\text{D}} \cdot \boldsymbol{p} + \sqrt{\frac{1-\kappa}{2}} A\, \mathrm{e}^{-j\omega(t)(t-\tau_{\text{R}})}\right]\boldsymbol{p}, \tag{10}$$

where $\boldsymbol{R}_{\text{R},s}$ and $\boldsymbol{R}_{\text{R},p}$ align the polarization of the reference to the polarizations $\boldsymbol{s}$ and $\boldsymbol{p}$.

Assuming square law detectors with a photocurrent proportional to the incident field according to $i(\omega) = \mathcal{R}\,|\boldsymbol{E}|^2$, where $\mathcal{R}$ is the responsivity of the photodetector, the difference currents produced by the balanced photodetectors are easily seen to be sums of the transfer function elements $\hat{H}_{k,l}$ with different delays

$$i_s = \mathcal{R}\,|A|^2\, \frac{\sqrt{\kappa}}{N}\frac{\sqrt{1-\kappa}}{\sqrt{2}} \sum_{k,l=1}^{N} \mathrm{Re}\Big[\left(s_1\hat{H}_{2k-1,2l-1} + s_2\hat{H}_{2k,2l-1}\right) \mathrm{e}^{-j\omega(t)(\tau_{\text{R}}-\tau_{\text{out},k}-\tau_{\text{in},l})} + \left(s_1\hat{H}_{2k-1,2l} + s_2\hat{H}_{2k,2l}\right) \mathrm{e}^{-j\omega(t)(\tau_{\text{R}}-\tau_{\text{out},k}-\tau_{\text{in},l}-\tau_{\text{P}})}\Big] \tag{11}$$

$$i_p = \mathcal{R}\,|A|^2\, \frac{\sqrt{\kappa}}{N}\frac{\sqrt{1-\kappa}}{\sqrt{2}} \sum_{k,l=1}^{N} \mathrm{Re}\Big[\left(p_1\hat{H}_{2k-1,2l-1} + p_2\hat{H}_{2k,2l-1}\right) \mathrm{e}^{-j\omega(t)(\tau_{\text{R}}-\tau_{\text{out},k}-\tau_{\text{in},l})} + \left(p_1\hat{H}_{2k-1,2l} + p_2\hat{H}_{2k,2l}\right) \mathrm{e}^{-j\omega(t)(\tau_{\text{R}}-\tau_{\text{out},k}-\tau_{\text{in},l}-\tau_{\text{P}})}\Big]. \tag{12}$$

where s_i and p_i denote the components of $\boldsymbol{s}$ and $\boldsymbol{p}$ and stem from the inner product in Eq. (8).As the STL wavelength is swept, the different delays result in different wavelength offsets and thus the elements of the sums in Eqs. (11) and (12) appear at different frequencies in the spectra of i_s and i_p, allowing their extraction as discussed in the following section and thus allowing full characterization of the linear properties of the DUT.

2.2. Extraction of the device transfer function and linear parameters

The extraction of the complex time- and frequency domain transfer function matrices $\boldsymbol{h}(t)$ and $\boldsymbol{H}(\omega)$ from the recorded interferograms of Eqs. (11) and (12) requires a number of DSP steps as shown in Fig. 2 and discussed in sections 2.2.1 and 2.2.2. Further analysis of the transfer function matrix $\boldsymbol{H}(\omega)$ allows the extraction of a number of important linear parameters of the DUT, including insertion loss (IL), mode-dependent loss (MDL), differential modal group delay (DMD) and mode coupling [8, 21] and is discussed in section 2.2.3.

Optics EXPRESS

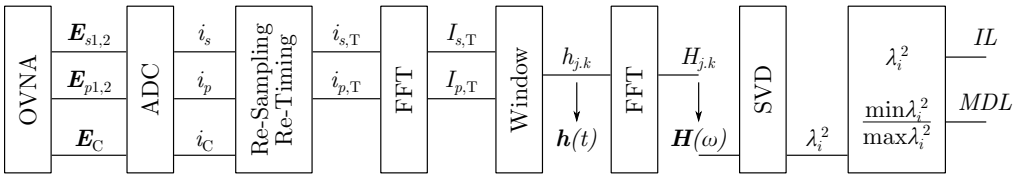

Fig. 2. Diagram of the signal processing flow for optical vector network analysis.

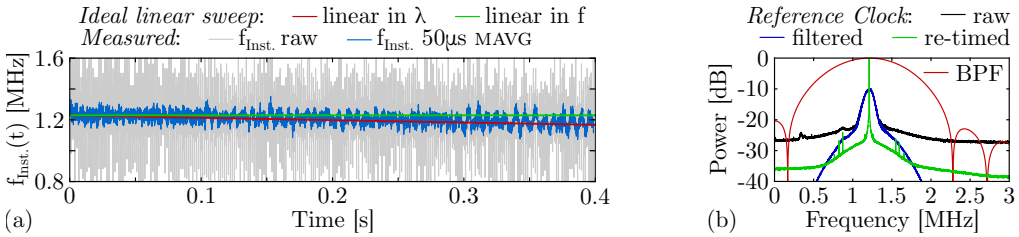

Fig. 3. Correction for sweep speed deviations and conversion from linear sweep in wavelength to linear sweep in frequency: (a) instantaneous frequency of the reference clock signal (MAVG: moving average), (b) normalized spectra of the reference clock signal before and after re-sampling and re-timing.

2.2.1. Linearization of the sweep

Prior to the extraction of the desired transfer function matrix elements from the interferograms of Eqs. (11) and (12), it is essential to correct for any deviations in the sweep speed during the linear wavelength sweep of the STL and to convert the latter into a linear sweep in frequency. The inclusion of the reference clock interferometer in the OVNA setup in Fig. 1 gives an additional signal

$$E_C = \sqrt{\frac{1-\kappa}{2}} A \left[e^{-j\omega(t)t} + e^{-j\omega(t)(t-\tau_C)} \right] \tag{13}$$

$$i_C = \mathcal{R} |A|^2 \, \mathrm{Re}\left[e^{-j\omega(t)\tau_C} \right], \tag{14}$$

where polarization alignment between the interferometer arms is assumed and polarization has thus been dropped in Eq. (13). This signal may be employed either as a clock signal for the analog to digital converter (ADC) [26], or as a reference signal to achieve linearization of the sweep in DSP, as discussed in this work.

A linear sweep in frequency would result in i_C containing only a single frequency, as the difference in fiber length between the two interferometer arms, and thus also the delay τ_C, is constant and known. In the experimentally acquired signal i_C, on the other hand, the sweep is linear in wavelength and the sweep speed is non-constant due to device limitations of the STL. Figure 3(a) shows the measured instantaneous frequency for a sweep across the optical C-band (1530 nm to 1570 nm) with a sweep speed of 100 nm/s and a path difference between the arms of the reference clock interferometer of 20 m. The obtained clock signal varies strongly in short time intervals, but with a moving average filter over 50 µs, falls within ±10 % of the calculated frequency resulting from an ideal linear sweep in wavelength.

Both the variation due to device imperfections and the frequency slope resulting from linear sweeping in wavelength may be corrected by upsampling the clock signal, selecting sampling points at given positions within each cycle—e.g., at all zero crossings—and subsequent re-timing of the selected samples to a constant sampling speed. Additionally filtering the clock signal around the desired frequency peak before re-sampling and re-timing improves the resulting

Optics EXPRESS

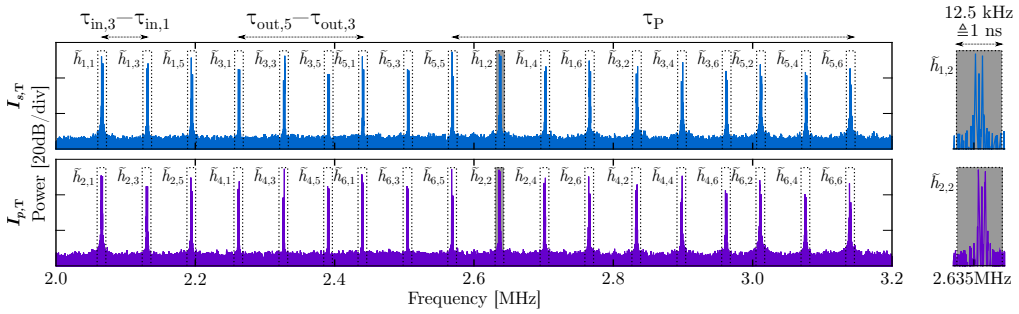

Fig. 4. Illustration of the windowing process, extracting the 36 elements $\tilde{h}_{k,l}(t)$ of the impulse response of a 3-mode DUT from the DFTs of the interferograms i_s and i_p.

signal. Figure 3(b) shows the normalized spectra of the reference clock signal before and after re-timing along with the applied filter. While in the spectrum of the raw signal the peak is spread into a wider peak due to the deviations from sweep speed, re-timing achieves a very narrow peak and thus good linearization of the sweep. Selecting samples of the interferograms of Eqs. (11) and (12) at the sampling points found from the reference clock signal and applying the same re-timing linearizes the underlying sweep and thus allows distortion-free extraction of the transfer function matrix elements.

2.2.2. Extraction of the device time and frequency response function matrices

Extraction of the complex time- and frequency domain transfer function matrices from the recorded interferograms is relatively straightforward, since, after linearization of the sweep, each delay results in a single, known frequency. Extracting the components of the sums at the different delays and combining them into 2×2 sub-matrices for each $\{k, l\}$ as

$$\begin{aligned}\begin{bmatrix} s_1\hat{H}_{2k-1,2l-1} + s_2\hat{H}_{2k,2l-1} & s_1\hat{H}_{2k-1,2l} + s_2\hat{H}_{2k,2l} \\ p_1\hat{H}_{2k-1,2l-1} + p_2\hat{H}_{2k,2l-1} & p_1\hat{H}_{2k-1,2l} + p_2\hat{H}_{2k,2l} \end{bmatrix} &= \begin{bmatrix} s_1 & s_2 \\ p_1 & p_2 \end{bmatrix} \begin{bmatrix} \hat{H}_{2k-1,2l-1} & \hat{H}_{2k-1,2l} \\ \hat{H}_{2k,2l-1} & \hat{H}_{2k,2l} \end{bmatrix} \\ &= \boldsymbol{R}_{s,p} \begin{bmatrix} \hat{H}_{2k-1,2l-1} & \hat{H}_{2k-1,2l} \\ \hat{H}_{2k,2l-1} & \hat{H}_{2k,2l} \end{bmatrix} = \begin{bmatrix} \tilde{H}_{2k-1,2l-1} & \tilde{H}_{2k-1,2l} \\ \tilde{H}_{2k,2l-1} & \tilde{H}_{2k,2l} \end{bmatrix}, \end{aligned} \tag{15}$$

shows that the PBS and subsequent polarization-diverse detection may be regarded as another polarization rotation on top of those in Eqs. (4) and (5); as $\boldsymbol{s}$ and $\boldsymbol{p}$ are orthogonal unitary vectors, their elements s_1, s_2, p_1 and p_2 together form a unitary basis and thus the matrix $\boldsymbol{R}_{s,p}$ is a unitary matrix. To simplify discussion, this polarization rotation has further been combined with $\hat{\boldsymbol{H}}(\omega)$ by defining a matrix $\boldsymbol{R}_{\mathrm{N}s,p}$, similar in structure to $\boldsymbol{R}_{\mathrm{in}}$ and $\boldsymbol{R}_{\mathrm{out}}$ in Eqs. (4) and (5), i.e., being block-diagonal with N copies of $\boldsymbol{R}_{s,p}$, and defining $\tilde{\boldsymbol{H}}(\omega) = \boldsymbol{R}_{\mathrm{N}s,p}\boldsymbol{R}_{\mathrm{out}}\boldsymbol{H}(\omega)\boldsymbol{R}_{\mathrm{in}}$ with elements $\tilde{H}_{k,l}(\omega)$. These $\tilde{H}_{k,l}(\omega)$ differ from the elements $H_{k,l}(\omega)$ of the transfer function matrix of the DUT only by a series of polarization rotations, which have no impact on the linear parameters extracted from the transfer function matrix as discussed in section 2.2.3.

While the desired elements $\tilde{H}_{k,l}(\omega)$ appear in the interferograms of Eqs. (11) and (12), they can not be easily extracted in a direct manner. After performing a discrete Fourier transform (DFT) however, the elements $\tilde{h}_{k,l}(t)$ of the time domain transfer function, i.e., the impulse responses, may be directly extracted by simple windowing—provided the delays $\tau_{\mathrm{in},l}$, $\tau_{\mathrm{out},k}$ and τ_{P} were carefully selected to ensure sufficient separation to prevent any overlap of the impulse responses. Fig. 4 shows the windowing to extract the 36 elements $\tilde{h}_{k,l}(t)$ of the impulse response matrix from the DFTs of the two re-timed interferograms i_s and i_p of a 3-mode DUT.

Finally, the $\tilde{H}_{k,l}(\omega)$ are easily obtained by taking separate inverse DFTs of the $\tilde{h}_{k,l}(t)$ and thus the full time and frequency domain transfer function matrices $\tilde{\boldsymbol{h}}(t)$ and $\tilde{\boldsymbol{H}}(\omega)$ may be

reconstructed and further analyzed to derive the DUT linear parameters.

2.2.3. Calculation of the linear device parameters

Of the linear parameters associated with any SDM component or system, IL and MDL are likely the most important for SDM communication systems employing coherent detection and MIMO equalization [8]. The former determines power budgets thus limits available reach and the latter directly limits system capacity [7, 8]. Given the transfer function matrix $\tilde{\boldsymbol{H}}(\omega)$, both IL and MDL may be determined via singular value analysis [8]. The singular value decomposition (SVD) [28] decomposes $\tilde{\boldsymbol{H}}(\omega)$ into two unitary matrices $\boldsymbol{U}(\omega)$ and $\boldsymbol{V}(\omega)$ and a diagonal matrix $\boldsymbol{\Sigma}$ as

$$\tilde{\boldsymbol{H}}(\omega) = \boldsymbol{U}(\omega)\boldsymbol{\Sigma}(\omega)\boldsymbol{V}^{*}(\omega), \tag{16}$$

where * denotes the conjugate transpose and the diagonal elements $\lambda_1(\omega)$ to $\lambda_{2N}(\omega)$ of $\boldsymbol{\Sigma}(\omega)$ are the $2N$ singular values of $\tilde{\boldsymbol{H}}(\omega)$. The columns of the unitary input and output matrices $\boldsymbol{V}(\omega)$ and $\boldsymbol{U}(\omega)$ are the input and output eigenvectors of the system and describe the $2N$-dimensional polarization rotation (also referred to as mode-mapping, -mixing or -scrambling in the literature) between the launched input modes and the eigenmodes of $\tilde{\boldsymbol{H}}(\omega)$, and the latter and the received output modes respectively. Note that the singular values $\lambda_i(\omega)$ are the gains or losses associated with each eigenmode and their squares are equal to the eigenvalues of the phase-conjugate round-trip propagation matrix $\tilde{\boldsymbol{H}}(\omega)\tilde{\boldsymbol{H}}^{*}(\omega)$ [8, 11].

As the singular values $\lambda_i(\omega)$ are the gains/losses associated with the optical field, they directly relate to the insertion loss (IL) and mode-dependent loss (MDL) of the DUT. Defining the latter two in terms of optical power, IL is the mean of the squares of the singular values $\lambda_i(\omega)$, while MDL is the ratio between the maximum and minimum $\lambda_i^2(\omega)$:

$$IL = \overline{\lambda_i^2(\omega)} \qquad\qquad MDL = \frac{\max \lambda_i^2(\omega)}{\min \lambda_i^2(\omega)}. \tag{17}$$

Taking the SVD at each angular frequency ω yields the $\lambda_i(\omega)$ across the wavelength range of the STL sweep and thus allows wavelength resolved calculation of IL and MDL.

It should be noted that, for any unitary matrix, i.e., a lossless polarization rotation, the singular values are equal to 1 and thus the singular values of $\tilde{\boldsymbol{H}}(\omega)$ are the same as those of $\boldsymbol{H}(\omega)$, despite the series of polarization rotations the latter undergoes to become the former. The linear parameters derived via the SVD of $\tilde{\boldsymbol{H}}(\omega)$ are thus equal to those of the DUT.

Differential modal group delay (DMD) may impact system performance, given the presence of phase noise [15], and influences signal processing complexity as the maximum spread in group delays determines the minimum length of the MIMO equalizer [8]. DMD may be derived from $\tilde{\boldsymbol{H}}(\omega)$ by means of principle state of polarization analysis [11, 21, 29] where the principle delays are approximated by the eigenvalues of $\tilde{\boldsymbol{H}}(\omega + \Delta\omega)\tilde{\boldsymbol{H}}^{-1}(\omega)$ or by directly analyzing the impulse responses $\tilde{h}_{k,l}(t)$ [22, 25, 30]. In the latter case, distinct peaks for different mode groups $\tilde{h}_{k,l}(t)$ will be observed and DMD may be derived from the ratio of their respective spacing and the fiber length. Such analysis further allows the location and characterization of discrete events affecting mode-distribution along a fiber, by analyzing peaks at intermediate time instances [25]. Analysis of the impulse response is demonstrated in detail in section 3.2.

Finally, mode coupling may also be seen from analysis of the $\tilde{h}_{k,l}(t)$, where distributed mode coupling along the fiber will appear as plateaus between the peaks of the respective modes and mode coupling at discrete points generate additional peaks in the temporal response [22, 25, 30].

2.3. Optical vector network analyzer setup for reflective measurements

To characterize a single space division multiplexing (SDM) component, e.g., an SMUX, a transmissive measurement as shown in Fig. 1 may not be possible and a reflective measurement setup is

Optics EXPRESS

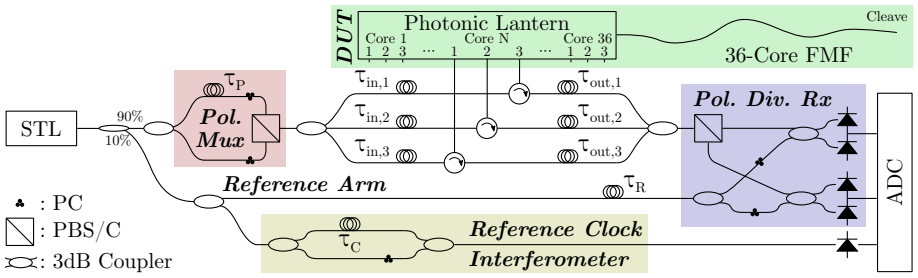

Fig. 5. SDM-OVNA setup for reflective measurement of the impulse response and transfer function of a 36-core 3-mode photonic lantern SMUX.

Table 1. Fiber configurations for the characterization of the photonic lantern and measurement of few-mode splice and cleaved fiber facet behavior.

Name	Pigtail	Splice	Fiber	Cleave	Angle
PL-CL0	0.3 m	–	–	CL0	0.7°
PL-SP1-CL1	1.3 m	SP1	8.8 m	CL1	0.4°
PL-SP2-CL1	0.3 m	SP2	8.8 m	CL1	0.4°
PL-SP2-CL2	0.3 m	SP2	8.7 m	CL2	0.9°

required. For such a measurement, the reflection from a cleaved fiber facet may be exploited, passing through the DUT a second time and being separated onto the output ports by circulators as shown in Fig. 5 for a 36-core 3-mode photonic lantern SMUX. For such a measurement, the measured response is the concatenation of the DUT, the fiber pigtail, the cleaved fiber facet (which for a good cleave is a weak mirror with a reflectivity of ca. 4 %), and again the fiber pigtail and DUT. While including the coupling to the fiber pigtail as part of the device response is usually desired, the effect of the reflection at the cleaved facet may be calibrated out of the measurement to allow measuring only the desired impulse response and complex transfer function of the fiber-coupled DUT.

3. Few-mode fiber, splice and component characterization

In this section we analyze a 3-mode multicore photonic lantern SMUX similar to that in [31], for with 36 cores. Based on the setup in Fig. 5, we show measurements results of system IL and MDL as well as fiber DMD and discuss the behavior of fusion splices in the 36-core FMF and that of the cleaved fiber facet itself. To this end a series of measurements was performed with different fiber configurations as shown in Table 1.

First, *PL-CL0* corresponds to measurement of the response of each of the photonic lanterns and serves as a base for comparison with the measurements with different splices and cleaves; the respective results are presented in section 3.1. *PL-SP1-CL1* additionally includes a fusion splice in the 36-core FMF and with different fiber lengths before and after the splice lends itself to analysis of the time-domain response; in section 3.2 the fiber DMD is calculated from the measured impulse responses and different degrees of mode-mixing are shown to be present at the splice for different cores. In *PL-SP2-CL1* the splice is replaced by another fusion splice, while maintaining the exact same configuration otherwise, including the cleave at which reflection takes place. This allows comparison of the system response with either splice to the base measurement and direct comparison of the system responses with the two splices; the respective results are discussed in section 3.3. Finally, *PL-SP2-CL2* introduces a different cleave to analyze the impact of cleave quality on the system response; this is discussed in section 3.4.

Optics EXPRESS

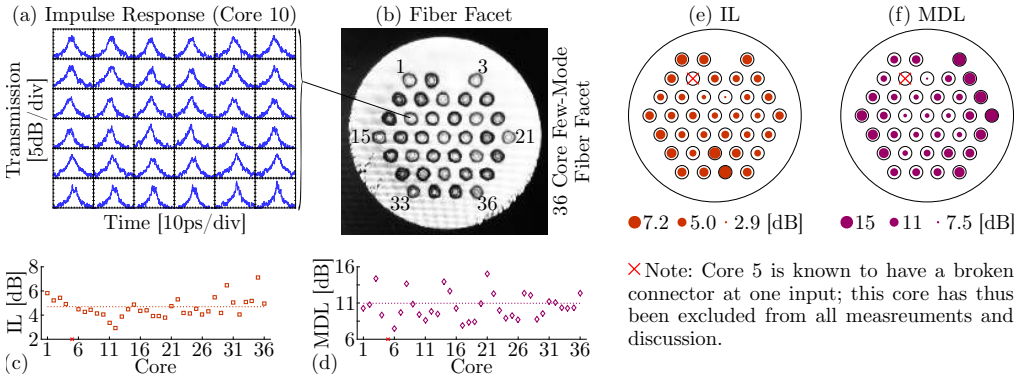

Fig. 6. Characteristics of the 36-core few-mode photonic lantern spatial multiplexer: (a) impulse response of core 10, (b) photograph of cleaved fiber facet with core numbering, (c) and (d) IL and MDL of all cores, (e) and (f) IL and MDL plotted across the fiber facet.

3.1. *Analysis of a 36-core 3-mode photonic lantern*

To characterize the 36-core photonic lantern SMUX, the full response for each of the 36 cores is measured separately, each yielding an impulse response matrix as shown in Fig. 6(a) for the exemplary case of core 10. While sufficient for the calculation of the complex transfer function and thus derivation of insertion and mode-dependent loss (IL and MDL), the impulse response hardly allows any differentiation of separate peaks due to the short fiber length of the pigtail, although it is significantly spread due to DMD.

Calculation of the complex transfer function and analysis of IL and MDL, as discussed in section 2.2, shows significant differences between cores for both IL and MDL as shown in Figs. 6(c) and 6(d), with the former ranging from 2.9 dB to 7.1 dB and the latter between 7.5 dB and 15.0 dB. It should be noted that the reported values are wavelength-averaged across the range of the optical C-band (1530 nm to 1570 nm) and that, in this and all of the following measurements of IL and MDL, the presented values have been corrected to account for the double-pass nature of the reflective measurement.

Analysis of the distribution of IL and MDL values of the fiber facet as shown in Figs. 6(e) and 6(f), shows the cores on the outer ring to have significantly higher IL and MDL as may be expected from increasing alignment error with increasing distance from the fiber center. Furthermore alignment between the photonic lantern chip and the output fiber pigtail seems to be optimum for cores slightly above and to the right of the center, rather than for the central cores, causing a generally increased misalignment.

3.2. *Few-mode fiber differential modal group delay*

Analysis of the impulse response matrix allows direct calculation of the DMD in the fiber, and in the presence of discrete mode-mixing points along the fiber, e.g., from fusion splices or the cleaved facet, further allows analysis of mode-mixing behavior at these points. Analyzing the impulse responses of measurement *PL-SP1-CL1*, which includes the SMUX, a 36-core FMF pigtail of 1.3 m length, a fusion splice and another 8.8 m of fiber, a number of well separated peaks can be seen in the impulse response matrices shown in Figs. 7(a)–7(c). In order to calculate the fiber DMD, the original of these peaks needs to be identified and once peaks corresponding to the mode-groups of interest have been selected, the DMD simply is the observed temporal spacing divided by the propagation distance in the fiber.

In the presence of discrete mode-mixing events, such as the fusion splice and cleave, additional peaks may arise due to different combinations of accumulated DMD before and after each mixing

Optics EXPRESS

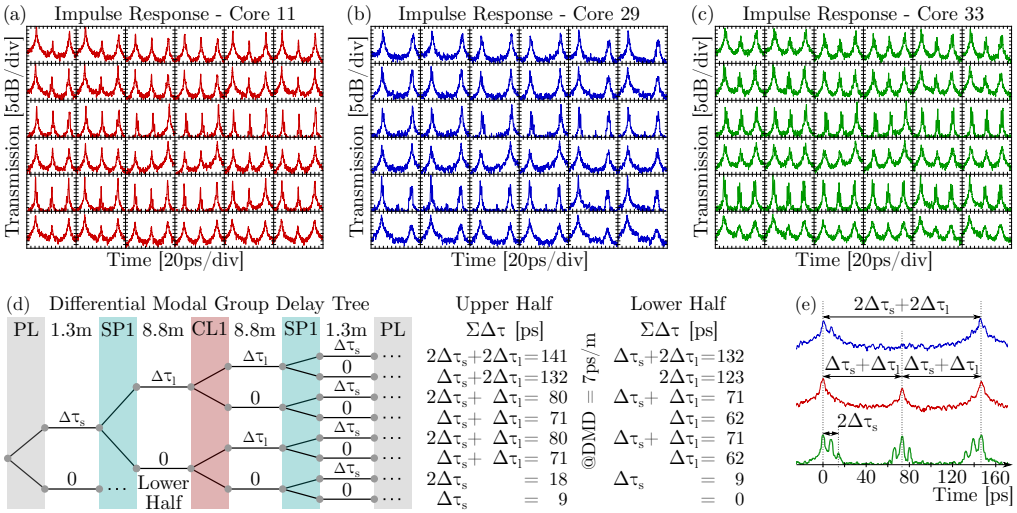

Fig. 7. Time domain analysis of the impulse responses from measurement *PL-SP1-CL1*. (a)–(c) Impulse response matrices of selected cores, showing different mode mixing behavior at the fusion splice and the cleave, (d) tree diagram of possible accumulated DMD assuming mode-mixing at discrete points and corresponding DMD values for all possible mode-mixing combinations, (e) comparison of the calculated values of accumulated DMD with experimentally obtained impulse responses.

event [25,30]. The impulse response matrices shown in Figs. 7(a)–7(c), corresponding to cores 11, 29 and 33 respectively, were selected as they represent three extreme cases in terms of mode-mixing at the splice and cleave. To interpret their differences, the possible accumulated delays with different mode mixing at the splice and cleave has to be considered.

Assuming a three-mode fiber supporting two mode groups with equal propagation constants within each mode group and different propagation constants between mode groups, Fig. 7(d) shows a tree diagram of all possible mode-mixing paths and associated accumulated relative delays. With the chosen fiber lengths, the delay $\Delta\tau_l$ is significantly larger than $\Delta\tau_s$ and thus three peaks around delays of 0, $\Delta\tau_l$ and $2\Delta\tau_l$ are expected. The outer peaks correspond to the two mode groups propagating without mixing, while the central peak corresponds to mixing at the cleave. The impulse response of core 11 in Fig. 7(a) shows such behavior with a strong central peak and thus significant mode mixing at the cleave. On the other hand, the impulse response of core 29 in Fig. 7(b) shows only two peaks, with the central peak missing, indicating that no mode mixing occurs at the cleave for this core. With no mode-mixing present, this core lends itself to simple calculation of the fiber DMD: the spacing of ca. 145 ps for the two cores and a total fiber distance of $2 \times (1.3\,\text{m} + 8.8\,\text{m})$ suggests a DMD of ca. 7 ps/m. Comparison of the impulse responses in Figs. 7(a) and 7(c), shows that in the latter case the three peaks are split into three sub-peaks each at a much closer spacing. Comparison of these spacings with the calculated spacings for a DMD of 7 ps/m in Fig. 7(d), confirms these spacings to result from mixing at the splice.

Comparing all the impulse responses as in Fig. 7(e), confirms a DMD of ca. 7 ps/m for the analyzed cores, which corresponds well with the DMD design of the fiber and previous measurements in [6, 24, 25], all of which suggest DMD values between 6.3 ps/m and 7.8 ps/m, depending on the core in question.

Besides providing a simple means to measure the fiber DMD parameters, time-domain analysis and comparison between the different impulse responses thus shows significantly different degrees of mode-mixing at the splice and cleave. While core 29 shows negligible mode-mixing at both the splice and cleave, core 11 shows significant mixing at the cleave, while showing none

Optics EXPRESS

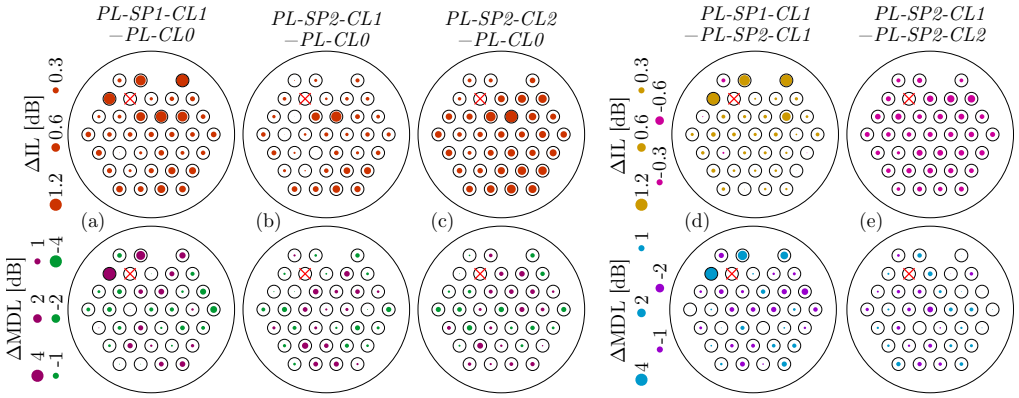

Fig. 8. Comparison of system IL and MDL with different splices and different cleaves: (a)–(c) ΔIL and ΔMDL for *PL-SP1-CL1*, *PL-SP2-CL1* and *PL-SP2-CL2* against *PL-CL0* respectively, (d) direct comparison of two splices, i.e., ΔIL and ΔMDL for *PL-SP2-CL1* against *PL-SP1-CL1*, (e) direct comparison of two cleaves, i.e., ΔIL and ΔMDL for *PL-SP2-CL1* against *PL-SP2-CL2*.

at the splice and finally core 33 shows strong mode-mixing at both. The remaining cores show less extreme behavior with varying degrees of mode-mixing at both points.

3.3. Few-mode fiber splice analysis

While some conclusions about the mode-mixing behavior at fusion splices in the 36-core 3-mode fiber may be drawn from analysis of the impulse response matrix as discussed in the previous section, analysis of their impact on system performance requires characterization of their influence on insertion and mode-dependent losses (IL and MDL). Two splices between the pigtail of the SMUX and an additional piece of 36-core FMF have been performed, resulting in measurements *PL-SP1-CL1* and *PL-SP2-CL1*. To directly show their impact on system IL and MDL, they are both compared to the measurement of the pigtailed SMUX alone (*PL-CL0*).

Figures 8(a) and 8(b) show the difference in wavelength-averaged IL and MDL for all cores for measurements with splice 1 and splice 2 compared to the measurement with only the SMUX. Both splices introduce significant IL, with a mean IL of 0.32 dB for splice 1 and 0.17 dB for splice 2. ΔIL is below 0.5 dB for all cores, but cores 11 and 12 for both splices and additionally cores 2, 3, 4 and 13 for splice 1. By analyzing the mean difference in system MDL, we observe that the inclusion of a fiber splice may in fact reduce overall system MDL, i.e., have a negative ΔMDL, if the mode-mixing at the splice happens to de-align previously aligned MDL elements (e.g., the MDL caused by the SMUX) or itself introduces MDL which is not aligned with the principle MDL axes, similar to what was previously reported in [16, 17, 19]. Changes in MDL are within ±2 dB for all cores, with the exception of cores 2 and 4 for splice 1. On average, across all cores, the splices increase MDL by a mean of 0.13 dB for splice 1 and 0.05 dB for splice 2, showing splice 2 to be of higher quality both in regards of IL and MDL.

Finally, Fig. 8(d) shows a direct comparison between the splices, confirming splice 2 to have persistently lower IL for almost all cores. Their impact on MDL however is largely similar, with the notable exceptions of cores 2, 3 and 4, which were the cores with high IL for splice 1, but good IL for splice 2.

3.4. Reflectivity at cleaved fiber facet analysis

The impact of the cleaved fiber facet itself on the IL and MDL of the system has been analyzed in a similar manner to the analysis of the impact of the fusion splices. Again two measurements

(*PL-SP2-CL1* and *PL-SP2-CL2*) were performed with identical fiber configuration except the element under study, i.e., the fiber cleave. The two compared fiber cleaves both produced high quality fiber facets, free of cracks or scratches across the whole range occupied by the 36-cores, however with slightly differing cleave angles of 0.4° for cleave 1 and 0.9° for cleave 2.

Figures 8(b) and 8(c) show the difference in IL and MDL for the two measurements with different cleaves when compared to the measurement of the SMUX alone. Cleave 2 shows a higher IL across all cores, with an average difference of 0.2 dB, as clearly seen in the direct comparison between the measurements with the two cleaves in Fig. 8(e). The impact on MDL observed between the two measurements with different cleaves is small, with the average difference between the two measurements negligibly small.

3.5. Discussion

By providing a complete set of reflective measurements, characterizing the photonic lantern SMUX on its own and measuring the impact of different splices and cleaves, while maintaining all other system and fiber configuration parameters, the presented method allows direct analysis of the impact of fiber splices in SDM systems. While comparative analysis of the IL of measurements with and without a splice provides a direct measurement of the splice IL, any obtained value of MDL is always relative to the surrounding system and does not measure the MDL associated only with the splice. This may appear to be a shortcoming of the reflective SDM-OVNA measurement, but in fact provides the more relevant information, as any isolated MDL measurement of a splice holds little information about the impact on system MDL—and thus system capacity. This is due to a) the fact that the MDL of a concatenation of elements with MDL strongly depends on the relative alignment between the eigenmodes of the elements, potentially resulting in significantly lower MDL for the chain than for the separate elements, and b) the fact that in any system splices will appear between elements with MDL and thus their polarization rotation (or mode-mixing) may impact system MDL significantly more than the MDL associated with the splice. Both these facts are visible in the measurements of section 3.3 by the difference in impact on MDL and the presence of cores with reduced MDL when including a splice. Analysis of the impact of fiber splices thus has to be of a qualitative or statistical nature and by providing measurements of two splices over 36 cores, the presented measurements show splices to introduce significant mode-mixing and cause changes in system MDL that are not necessarily correlated with splice IL.

The measurements of the impact of the cleave show changes in system MDL and IL at a non-negligible scale and thus serve to highlight the potential for a measurement uncertainty in any reflective OVNA measurement, unless analysis is performed by comparing measurements with the same cleaved fiber facet. While the impact on IL was found to be strongly correlated with the cleave angle, the average difference in MDL between measurements with different cleave angles was negligible.

4. Conclusions

In this work, a comprehensive discussion of spatially diverse optical vector network analysis was given, including the setup, principle of operation and necessary DSP required to fully characterize a space division multiplexing (SDM) system or component. Experimental characterization of a 108-channel photonic lantern spatial multiplexer (SMUX) coupled to a 36-core 3-mode fiber is demonstrated and employed as basis for measurement of the impact of splices in the fiber.

From the measured impulse response and complex transfer function matrices of the SMUX, we calculated IL, MDL and DMD, and found the SMUX to have an average IL of 4.7 dB and an average MDL of 11.0 dB, while the fiber has a DMD of 7 ps/nm. Using the SMUX as a base, the mode-mixing behavior of two different splices in the few-mode multi-core fiber (FM-MCF) was analyzed, finding large differences in the degree of mode-mixing for the different cores in each splice and for different splices. Analysis of the impact of the splices on system IL and MDL shows splices to

Optics EXPRESS

introduce significant IL with the better of the two splices showing an average increase in IL of 0.17 dB. As splices introduce significant-mode mixing, system MDL may be reduced or increased when including a splice, finding a change of MDL by ±2 dB. A similar analysis was performed for the cleaved fiber facet present in any reflective OVNA measurement, finding only a small difference in IL and MDL for different cleaves.

The presented measurements confirm spatially diverse optical network analysis to be a powerful tool for accurate characterization of SDM systems and components. By providing characterization of the behavior of splices in FM-MCF, it contributes to an improved modeling and capacity estimation of SDM systems with a large spatial channel count.

Funding

Det Frie Forskningsråd, Teknologi og Produktion (mmW-SPRAWL project).